



**QUEEN'S
UNIVERSITY
BELFAST**

Insight into the solar plage chromosphere with DKIST

Kuridze, D., Uitenbroek, H., Wöger, F., Mathioudakis, M., Morgan, H., Campbell, R., Fischer, C., Cauzzi, G., Schad, T., Reardon, K., da Silva Santos, J. M., Beck, C., Tritschler, A., & Rimmele, T. (2024). Insight into the solar plage chromosphere with DKIST. *The Astrophysical Journal*, 965(1), Article 15.
<https://doi.org/10.3847/1538-4357/ad2702>

Published in:
The Astrophysical Journal

Document Version:
Publisher's PDF, also known as Version of record

Queen's University Belfast - Research Portal:
[Link to publication record in Queen's University Belfast Research Portal](#)

Publisher rights

© 2024 The Authors.

This is an open access article published under a Creative Commons Attribution License (<https://creativecommons.org/licenses/by/4.0/>), which permits unrestricted use, distribution and reproduction in any medium, provided the author and source are cited.

General rights

Copyright for the publications made accessible via the Queen's University Belfast Research Portal is retained by the author(s) and / or other copyright owners and it is a condition of accessing these publications that users recognise and abide by the legal requirements associated with these rights.

Take down policy

The Research Portal is Queen's institutional repository that provides access to Queen's research output. Every effort has been made to ensure that content in the Research Portal does not infringe any person's rights, or applicable UK laws. If you discover content in the Research Portal that you believe breaches copyright or violates any law, please contact openaccess@qub.ac.uk.

Open Access

This research has been made openly available by Queen's academics and its Open Research team. We would love to hear how access to this research benefits you. – Share your feedback with us: <http://go.qub.ac.uk/oa-feedback>



Insight into the Solar Plage Chromosphere with DKIST

David Kuridze¹, Han Uitenbroek¹, Friedrich Wöger¹, Mihalis Mathioudakis², Huw Morgan³, Ryan Campbell², Catherine Fischer¹, Gianna Cauzzi¹, Thomas Schad¹, Kevin Reardon¹, João M. da Silva Santos¹, Christian Beck¹, Alexandra Tritschler¹, and Thomas Rimmele¹

¹ National Solar Observatory, 3665 Discovery Drive, Boulder, CO 80303, USA; dkuridze@nso.edu

² Astrophysics Research Centre, School of Mathematics and Physics, Queen's University Belfast, Belfast BT7 1NN, UK

³ Department of Physics, Aberystwyth University, Ceredigion, SY23 3BZ, UK

Received 2023 November 28; revised 2024 February 1; accepted 2024 February 5; published 2024 April 1

Abstract

The strongly coupled hydrodynamic, magnetic, and radiation properties of the plasma in the solar chromosphere make it a region of the Sun's atmosphere that is poorly understood. We use data obtained with the high-resolution Visible Broadband Imager (VBI) equipped with an $H\beta$ filter and the Visible Spectro-Polarimeter (ViSP) on the Daniel K. Inouye Solar Telescope to investigate the fine-scale structure of the plage chromosphere. To aid in the interpretation of the VBI imaging data, we also analyze spectra from the CHROMospheric Imaging Spectrometer on the Swedish Solar Telescope. The analysis of spectral properties, such as enhanced line widths and line depths, explains the high contrast of the fibrils relative to the background atmosphere demonstrating that $H\beta$ is an excellent diagnostic for the enigmatic fine-scale structure of the chromosphere. A correlation between the parameters of the $H\beta$ line indicates that opacity broadening created by overdense fibrils could be the main reason for the spectral line broadening frequently observed in chromospheric fine-scale structures. Spectropolarimetric inversions of the ViSP data in the Ca II 8542 Å and Fe I 6301/6302 Å lines are used to construct semiempirical models of the plage atmosphere. Inversion outputs indicate the existence of dense fibrils in the Ca II 8542 Å line. The analyses of the ViSP data show that the morphological characteristics, such as orientation, inclination, and length of fibrils, are defined by the topology of the magnetic field in the photosphere. Chromospheric maps reveal a prominent magnetic canopy in the area where fibrils are directed toward the observer.

Unified Astronomy Thesaurus concepts: [Solar chromosphere \(1479\)](#); [High resolution spectroscopy \(2096\)](#); [Plages \(1240\)](#); [Radiative transfer \(1335\)](#); [Solar fibrils \(532\)](#); [Ground-based astronomy \(686\)](#)

1. Introduction

The highly inhomogeneous nature of the solar chromosphere was discovered in the second half of the 19th century by Father Angelo Secchi, who reported the existence of *vertical flames* seen at the solar limb (Secchi 1877), which are now called spicules (Roberts 1945). This makes chromospheric fine-scale structures one of the oldest scientific topics in solar physics.

Some major breakthroughs in our understanding of spicules, and their on-disk counterparts, mottles, were made with the commissioning of half-meter class solar telescopes equipped with narrowband filters and spectrographs able to perform simultaneous imaging and spectroscopic observations (see the reviews by Beckers 1968, 1972). Such data made it possible to perform the first high-resolution measurements of spicule characteristics such as morphology, thermodynamical properties, spectral characteristics, etc. The seeing-free broadband imaging provided by the Solar Optical Telescope (SOT) on board Hinode and the adaptive optic systems installed on 1 m class solar telescopes equipped with Fabry–Pérot interferometers such as the Swedish Solar Telescope (SST), the Dunn Solar Telescope, and the Goode Solar Telescope have further advanced our understanding of the chromosphere at fine scales. For example, the data obtained from these telescopes have identified more energetic, and short-lived features such as type II spicules (de Pontieu et al. 2007) and their on-disk

counterparts, rapid excursions (Langangen et al. 2008; Rouppe van der Voort et al. 2009; Kuridze et al. 2015).

Still, many aspects of the fine-scale chromospheric structures, including their magnetic field strength and topology, thermodynamical properties, and formation mechanisms remain poorly understood (Sterling 2000; Tsiropoula et al. 2012). The reasons for this are manyfold, and include (i) the very dynamic nature of spicular structures, with spatial and temporal scales close to the resolution of present-day solar telescopes; (ii) the large number of structures that appear to overlap; (iii) the inherently low signal-to-noise ratios (S/Ns) of polarimetric data sets in the chromosphere (Trujillo Bueno & del Pino Alemán 2022); (iv) the challenges associated with the modeling and interpretation of chromospheric spectral lines that rely on solving the complex non-LTE (i.e., departures from local thermodynamic equilibrium) radiative transfer problem (de la Cruz Rodríguez & van Noort 2017; Beck et al. 2019; Carlsson et al. 2019; Kuridze et al. 2021; Kriginsky et al. 2023).

Chromospheric fine-scale fibrillar structures are intricately connected to the local magnetic field distribution and are thought to act as tracers for the local magnetic field topology, much like apparent coronal loops are used as proxies for the magnetic field in the lower corona (Prasad et al. 2022). In the quiet Sun (QS) network, chromospheric fine structures create rosettes (*bushes*), which are clusters of elongated mottles expanding radially around a common center over internetwork regions. Active regions (ARs) are characterized by an increased number of magnetic elements producing a large number of fine-scale, elongated features, referred to as fibrils when on the disk. Some of the most interesting fibril-dominated ARs are plages.

These are regions created by mostly unipolar, almost radial kilogauss fields in the photosphere that appear as bright areas, called faculae, in photospheric lines (see, e.g., Spruit 1976; Keller et al. 2004; Rezaei et al. 2007). The resemblance has been reported between QS mottles and plage fibrils (see the review by Tsiropoula et al. 2012). Foukal (1971a) investigated the morphological relation between chromospheric fine structures observed in regions with different magnetic activity. By comparing the observed parameters of fine-scale chromospheric structures they concluded that there is a continuous morphological progression between QS spicules/mottles and AR/plage fibrils. Foukal (1971a) found that spicules/mottles in QS bushes are less inclined with respect to the normal of the surface, while AR/plage fibrils are mostly horizontal. The reason for this is that the larger deflection of the magnetic field in plage creates a relatively lower-lying horizontal canopy in the chromosphere. In a follow-up study, Foukal (1971b) concluded that fibrils are longer than mottles, with stronger magnetic field strengths, but similar temperatures and densities. Similar morphological properties of plage fibrils have been reported by Pietarila et al. (2009), who analyzed a high-resolution Ca II K filtergram of an AR plage recorded by the SST at the disk center (DC). Anan et al. (2010) analyzed broadband Ca II H filtergrams of a plage region close to the limb obtained by Hinode/SOT and found that spicular jets are shorter in the plage than the QS limb spicules, and are characterized by ballistic motions under constant deceleration.

The strength and local inclination angle of the magnetic field in plage magnetic flux concentrations (MFCs) have long been studied using spectropolarimetric observations. Inversions of photospheric spectral lines infer kilogauss field strengths in the plage oriented mostly parallel to the solar normal. Inclinations from the local vertical by up to 10° – 20° have also been reported (Topka et al. 1992; Bernasconi et al. 1995; Martínez Pillet et al. 1997; Buehler et al. 2015, 2019). By inverting the chromospheric He I 10830 Å line together with the adjacent photospheric Si I 10827 Å line, Anan et al. (2021) found vertically oriented MFCs in the plage photosphere that changed direction, becoming nearly horizontal in the chromosphere. Using Ca II 8542 Å observations, Pietrow et al. (2020) inferred the magnetic field strength of an MFC in the plage chromosphere as 450 G, with an inclination of $\sim 16^{\circ}$. Using full Stokes observations in the Mg I 5173, Na I 5896, and Ca II 8542 Å lines, Morosin et al. (2020) found that the photospheric magnetic field in the plage region was expanding horizontally toward the chromosphere and forming a volume-filling canopy. They derived a value of ~ 658 G for the mean total magnetic field strength of the plage canopy in the chromosphere using weak field approximation (WFA) techniques. From the analysis of some of the chromospheric data used in this paper, and using WFA, da Silva Santos et al. (2023) derive an average magnitude of the line-of-sight (LoS) chromospheric magnetic field in the plage of approximately -210 G, with clear variations among the fibrils surrounding the plage patches.

One of the main spectral characteristics of chromospheric fine-scale fibrillar structures in strong chromospheric spectral lines is their broader line width relative to the background atmosphere. The causes of this line broadening still constitute a challenge. The combination of multi-instrument, multiwavelength optical, and UV observations has provided evidence that there are transition region (TR) and coronal signatures occurring cospatially and cotemporally with chromospheric

fine structures (De Pontieu et al. 2011; Madjarska et al. 2011; Henriques et al. 2016), suggesting that thermal broadening could be a dominant mechanism of the increased line width in spicular structures. However, this remains a controversial subject (see, e.g., Beck et al. 2016). Nonthermal broadening mechanisms have also been investigated to explain the enhanced line width of spicular jets (Erdélyi & Fedun 2007; Jess et al. 2009; Zaqarashvili & Erdélyi 2009; Kuridze et al. 2012, 2016).

In this paper, we use data obtained with the high-resolution Visible Broadband Imager (VBI; Wöger et al. 2021) and Visible Spectro-Polarimeter (ViSP; de Wijn et al. 2022) on the recently commissioned Daniel K. Inouye Solar Telescope (DKIST; Rimmele et al. 2020) to investigate the fine-scale structure of a plage chromosphere. We were able to observe a large field of view (FoV) and resolve fine-scale structures of the chromosphere in broadband $H\beta$ filtergrams. To aid in the interpretation of the VBI/ $H\beta$ data, we also analyze $H\beta$ scans obtained with the CHROMospheric Imaging Spectrometer (CHROMIS) on the SST. Furthermore, we inverted Stokes profiles obtained with the ViSP instrument in the Fe I 6301/6302 Å and Ca II 8542 Å lines with the Departure coefficient aided Stokes Inversion based on Response functions (DeSIRE; Ruiz Cobo et al. 2022) code and investigated the connection between the plage magnetic field and the fibrils' characteristics.

2. Observations and Data Reduction

2.1. DKIST Observational Setup

The observations used in this paper were obtained between 17:09 and 19:20 UT on 2022 June 3 with the VBI (Wöger et al. 2021) and ViSP (de Wijn et al. 2022) deployed at the DKIST (Rimmele et al. 2020) under good seeing conditions. The telescope was sequentially pointed at four adjacent positions to cover a large plage region located at the southeast part of the full solar disk. The heliocentric coordinates of the center of the full FoV covered by the observations were $(x, y) = (-362'', -406'')$, with heliocentric angle $\mu \approx 0.843$ (see Figure 1). Details about the data and instrumentation are given in the next subsections, and in Table 1.

2.1.1. ViSP Data

At each telescope pointing, the ViSP spectropolarimeter performed a large raster scan with the $0''.2142$ wide slit oriented along the solar north–south direction. Each scan consisted of 490 slit positions separated by a slit step of $0''.219$, with a time step of 3.3 s, for a total observing time of about 27 minutes per scan. Arms 1 and 3 of the spectrograph were used to observe the spectral ranges 6295.2–6307.8 and 8535.4–8544.9 Å, respectively (arm 2 was not used for these observations). The spatial samplings along the slit for arm 1 and arm 3 are $0''.0298$ and $0''.0194 \text{ pixel}^{-1}$, with a slit length of $\sim 75''$ and $48''$, respectively. Hence, the FoV of each raster scan covered $107'' \times 75''$ for arm 1 and $107'' \times 48''$ for arm 3 (Table 1). The spectral sampling for arms 1 and 3 were 0.0128 and $0.0188 \text{ Å pixel}^{-1}$.

The polarimetric modulation consisted of 10 modulation states that were repeatedly observed 12 times each, at a camera frame rate of 41 Hz and with an exposure time of 4 ms for both cameras. The data were processed to level 1 using version 2 of the ViSP data reduction pipeline, which includes polarimetric calibration to obtain the full Stokes vector. Additional crosstalk corrections were applied based on the method developed by

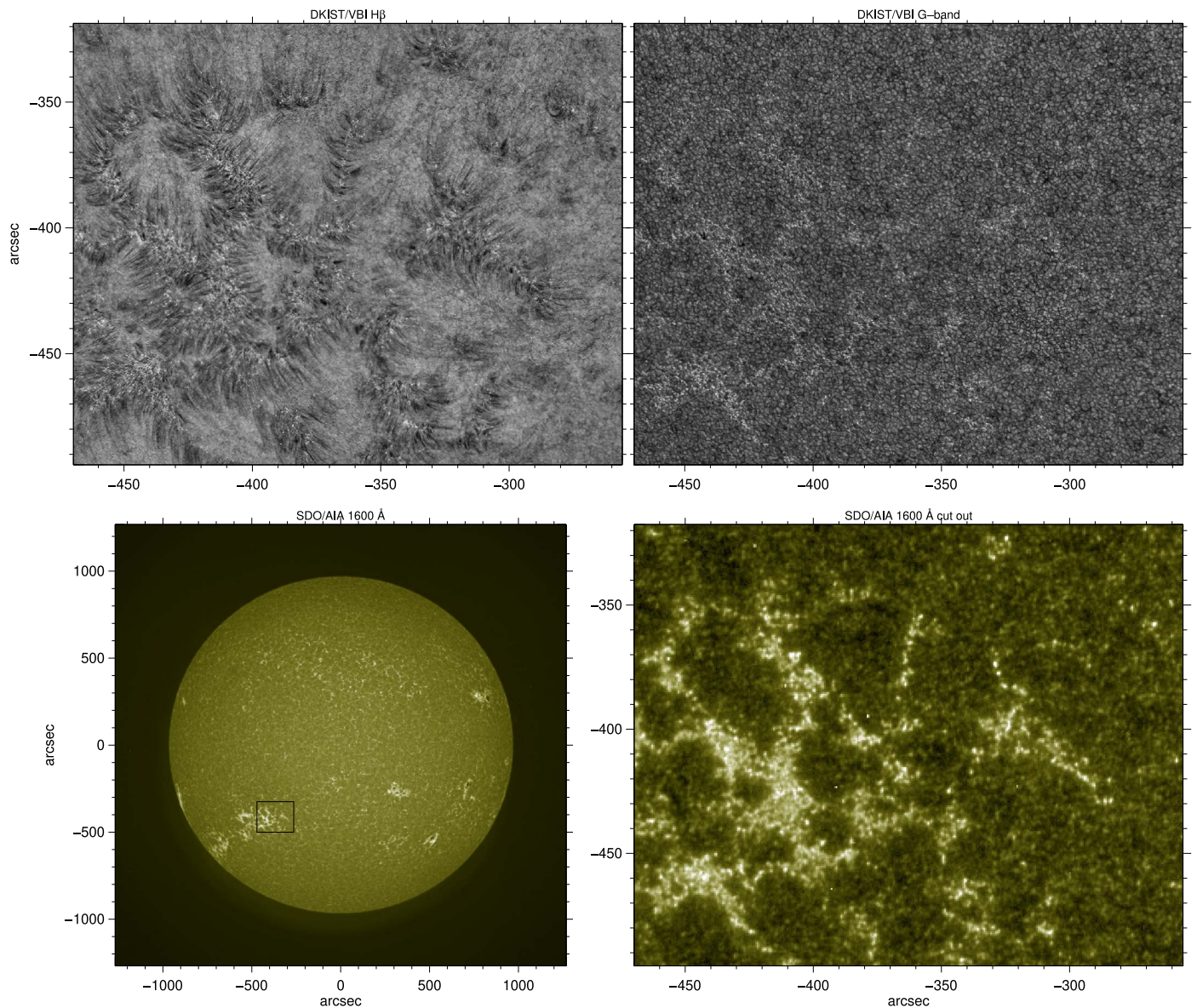


Figure 1. Overview of the DKIST observations of the plage. Top row: mosaics of high-resolution $H\beta$ (left panel) and G -band (right panel) filtergrams obtained with the VBI instrument on 2022 June 3 between 17:10 and 19:20 UT. Bottom left: a context AIA 1600 Å passband full-disk image taken on 2022 June 3 at 16:40 UT. The black box indicates the plage region observed with DKIST. Bottom right: a cutout of the 1600 Å image coaligned with the DKIST/VBI FoV.

Table 1
Summary of the DKIST Instruments and Data Used in This Work

Start Time UT	Instrument	Filter/Arm	Wavelength Range (Å)	Spatial Sampling	Instantaneous FoV	Time Step	Sampled FoV	Full Map Time	Number of Maps
17:10:50	VBI	Blue	$H\beta$ at 4861.13	0''011	45'' × 45''	3 s	115'' × 115''	27 s	20
17:10:22	VBI	Blue	G band at 4305	0''011	45'' × 45''	3 s	115'' × 115''	27 s	20
17:09:55	ViSP	arm 1	6295.2–6307.8	0''0298 ^a	0''2142 ^b × 75''	3.3 s	107'' × 75''	27 min	1
		arm 3	8535.4–8544.9	0''0194 ^a	0''2142 ^b × 48''	3.3 s	107'' × 48''	27 min	1

Notes. Values refer to a single telescope pointing.

^a Pixel scale along the slit

^b Width of the slit

Jaeggli et al. (2022). More details on the data post-processing can be found in da Silva Santos et al. (2023).

The raster scans at the four different telescope pointings are then stitched together to produce large mosaics (Figure 2) of

the observed plage region. Figure 2 shows full maps of Fe I 6302 Å net (wavelength-integrated) Stokes Q , U , and V coaligned with a cutout of the Helioseismic and Magnetic Imager (HMI) LoS magnetogram. Polarization maps indicate

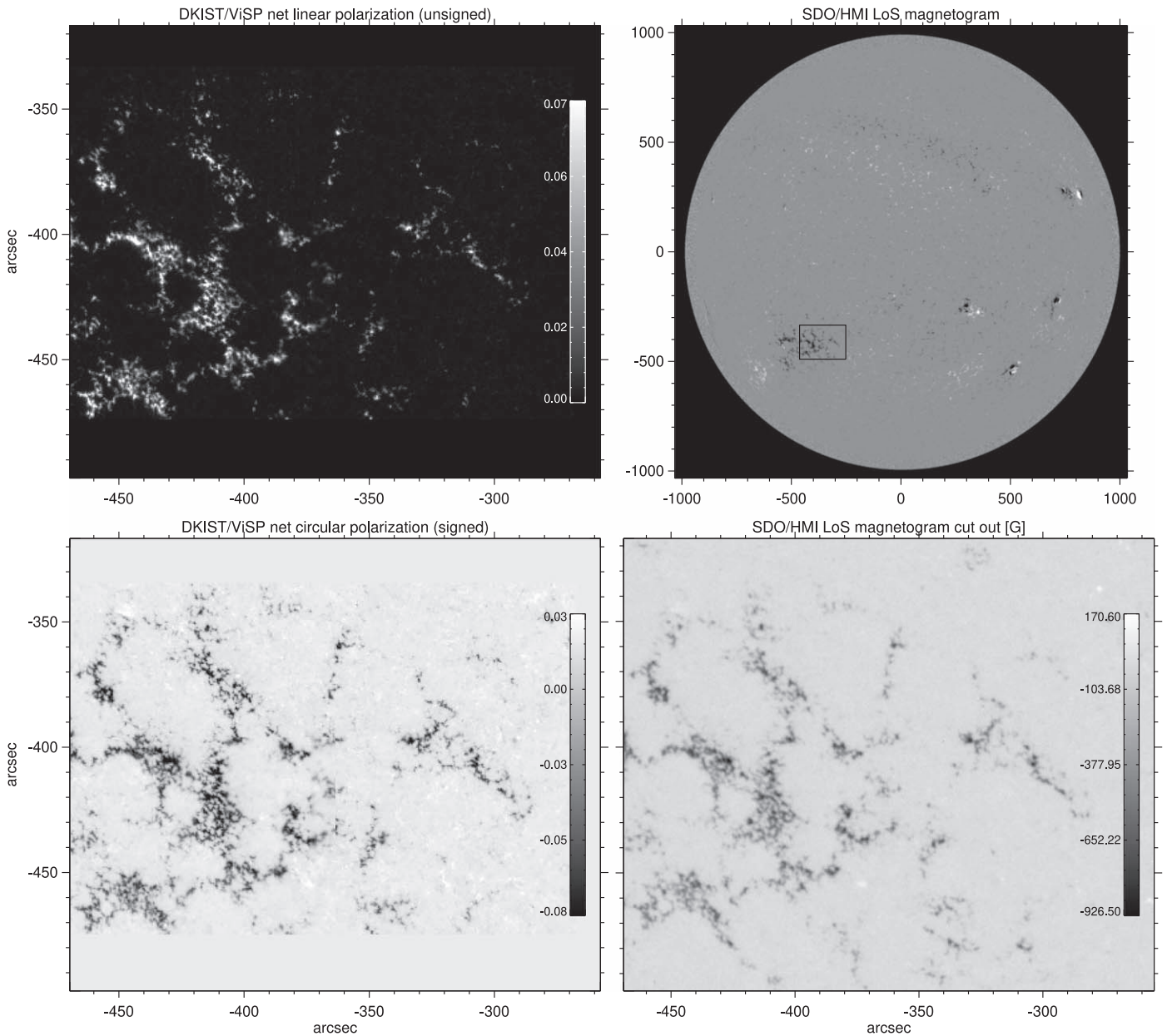


Figure 2. Left column: composite ViSP net linear (top panel) and circular (bottom panel) polarization images compiled from four different scans in adjacent positions. The Stokes Q , U , and V parameters are integrated over $\Delta\lambda = \pm 0.17 \text{ \AA}$ from the line core rest wavelength of the Fe I 6302 \AA line. Top right: a context LoS magnetogram of the full Sun in the Fe I 6173 \AA passband obtained with HMI. The black box indicates the plage region observed by DKIST. Bottom right: a cutout of the HMI image coaligned with the DKIST FoV.

that the observed region is a highly unipolar plage without a sunspot. However, the Stokes V map shows many small-scale parasitic polarity elements that are not resolved in the HMI magnetogram (bottom panels of Figure 2).

2.1.2. VBI Data

During each ViSP raster scan, we used the VBI blue branch to obtain filtergrams in the G band, Ca II K, and $H\beta$. The wavelengths are selected sequentially using interference filters mounted on a rotating filter wheel, and the full width half-maximum (FWHM) of the filters are approximately 4.37 ± 0.048 , 1.01 ± 0.02 , and $0.464 \pm 0.01 \text{ \AA}$ for the G band, Ca II K, and $H\beta$, respectively (Wöger 2014). Single exposure times were ~ 0.7 , 25, and 4 ms for the G band, Ca II K, and $H\beta$ with a

frame rate of up to 30 Hz. In the following, we limit our analysis to G -band and $H\beta$ data.

The instantaneous FoV of VBI blue is $45'' \times 45''$ with a spatial sampling of $0''.011 \text{ pixel}^{-1}$. For these observations, we employed the so-called *field-sampling mode* to cover the full DKIST FoV of $2' \times 2'$ with a mosaic of 3×3 tiles. This fully covers the field sampled by ViSP during the raster (see Figure 1 in da Silva Santos et al. 2023). All VBI images were reconstructed using the speckle code of Wöger et al. (2008) to remove residual atmospheric distortion from the data, bringing the effective time step to 3 s per tile. Hence, at any given wavelength (filter), the full DKIST FoV was sampled in 27 s, and the overall cadence for the three filters' sequence was 81 s. For each telescope pointing, the sequence was repeated 20 times, for a duration of ~ 27 minutes, i.e., the duration of the

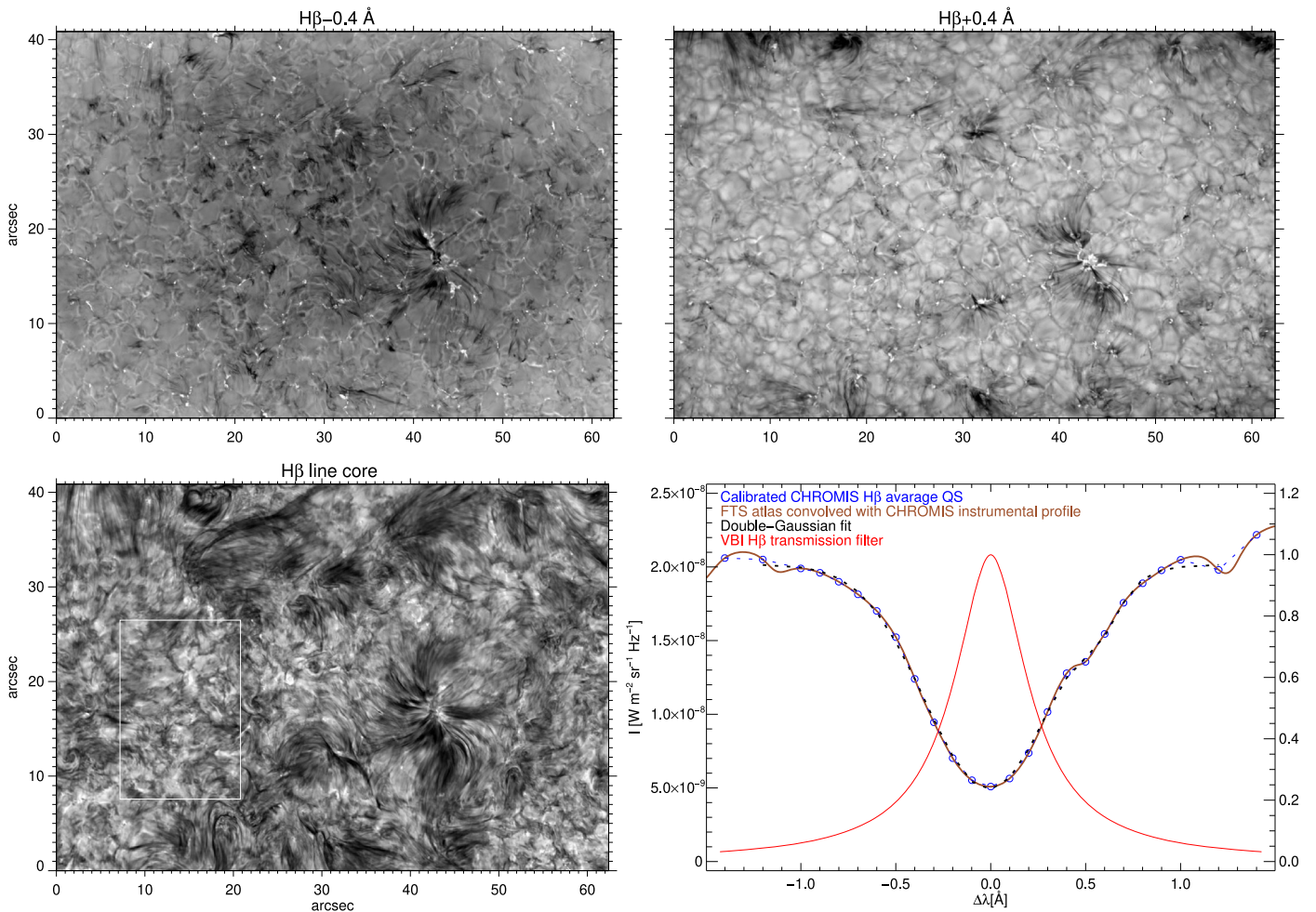


Figure 3. Overview of the SST data. Monochromatic $H\beta$ line wing (top row) and core (bottom left) images obtained with the CHROMIS instrument at 10:47 UT on 2019 August 3 at the DC. The bottom right panel displays the experimental transmission profile of the VBI filter (red line, right axis) and the CHROMIS $H\beta$ average line profile (dashed blue line) calculated for a QS region marked with the white box in the bottom left panel. Circles show the spectral positions selected for the CHROMIS line scan. The dashed black line represents the double-Gaussian fit of the average profile. The brown line represents the FTS atlas profile convolved with the CHROMIS instrumental profile.

ViSP raster scan. Adjacent tiles in the VBI field-sampling mode have overlaps of about $7''$, and were stitched with sub-pixel accuracy using the World Coordinate System header information and cross-correlation techniques. The intensity in overlapping areas is taken as the average at each location.

Finally, these 3×3 mosaics obtained at each of the four different telescope pointings were stitched together to produce a large mosaic covering the plage region. Adjacent meta-tiles have overlaps of about $20''$ resulting in an overall FoV of about $175'' \times 205''$ (Figure 1). Figure 1 is produced using the tiles with the best spatial resolution.

As mentioned above, seeing conditions were good throughout the observations. After reconstruction, we estimate that multiple frames achieved a spatial resolution close to the diffraction limit ($0''.022$ at 430 nm), as determined by the size of the smallest resolved structures seen in the data.

2.2. Solar Dynamics Observatory Data

We also analyze observations of the same region obtained with NASA’s Solar Dynamics Observatory (SDO) Atmospheric Imaging Assembly (AIA; Lemen et al. 2012) in its 1600 Å channel and the HMI (Scherrer et al. 2012) magnetograms in FeI 6173 Å. The SDO observations provide

full Sun context imaging and allow a comparison with the DKIST data. SDO images are coaligned with the DKIST/VBI/ViSP data set using the SolarSoft *auto_align_images* function via cross correlation.

2.3. SST/CHROMIS Data

Since the VBI data lack fine spectral resolution, we use data obtained with the CHROMIS dual Fabry–Pérot interferometer installed on the SST (Scharmer et al. 2003; Scharmer 2017) to further investigate the spectral characteristics of chromospheric fine-scale structures in $H\beta$. Observations were undertaken between 10:47 and 11:04 UT on 2019 August 3 in a quiet area at the DC. The data set includes narrowband spectral imaging in $H\beta$ with a spatial sampling of $0''.0378 \text{ pixel}^{-1}$ and a FoV of about $62'' \times 41''$. Many images in the time series were observed under extremely good seeing conditions, with a spatial resolution close to the diffraction limit of the telescope, which is $\sim 0''.13$ at this wavelength. The $H\beta$ line scan consists of 25 profile samples ranging from -1.2 to $+1.2$ Å (Figure 3) from the line center. CHROMIS spectral resolution (transmission profile FWHM) is 0.1 Å at 4860 Å. A full spectral scan had an acquisition time of 7 s. The data were processed using the

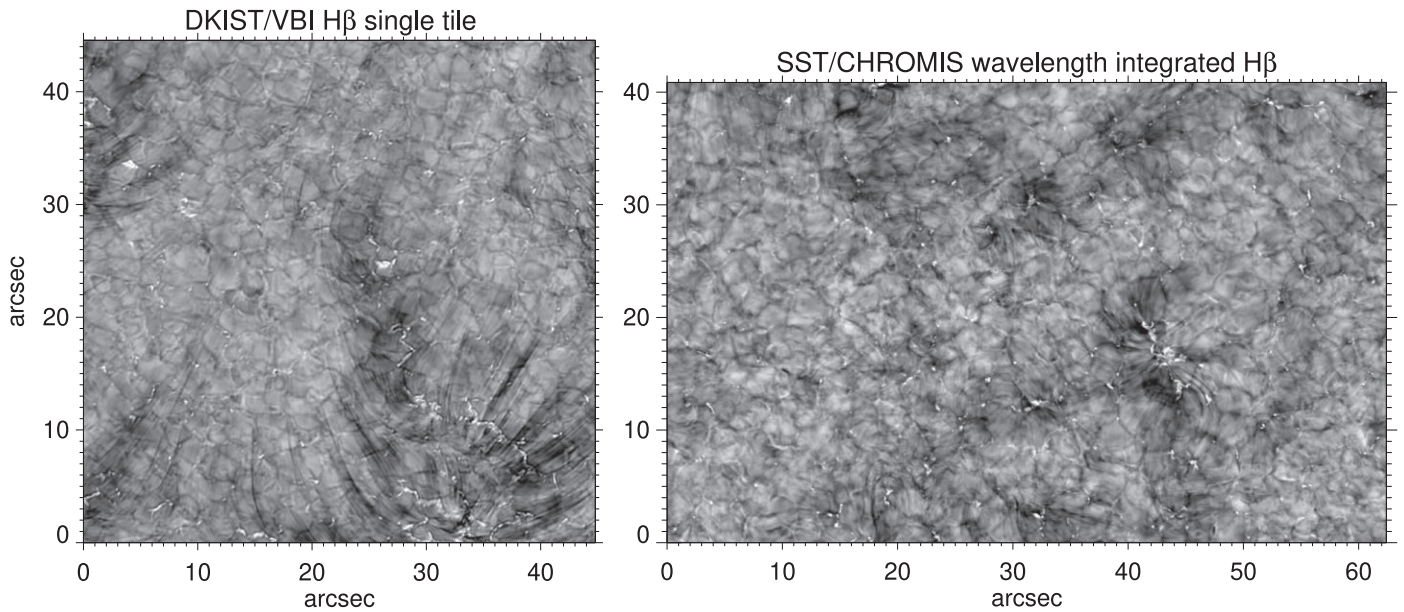


Figure 4. A qualitative comparison of the DKIST VBI image (left panel) and the wavelength-integrated SST CHROMIS (right panel) $H\beta$ image. Before integrating over wavelength, the CHROMIS spectral scan is multiplied by the VBI transmission filter. The DKIST FoV covered by the presented tile is located at around $(x, y) = (-340'', -370'')$ in the context image presented in Figure 1, whereas the CHROMIS FoV is located at the DC; they are thus neither cospatial nor cotemporal.

CHROMISRED reduction pipeline, which includes MOMFBD image restoration (Van Noort et al. 2005; Löfdahl et al. 2021).

The pipeline also applied spectral intensity calibration to remove the effect of the prefilter transmission profiles and scale intensity counts to SI units. However, the position angle of the science data is not taken into account during the calibration (Löfdahl et al. 2021).

For recalibrating CHROMIS $H\beta$ data we used a spatially averaged profile over the DC, QS area marked with a white rectangle in Figure 3 ($I_{av}(\lambda)$). The Fourier Transform Spectrometer (FTS) atlas $H\beta$ profile ($I_{FTS}(\lambda)$) (Neckel 1999) convolved with the CHROMIS instrumental profile was used as the calibration reference. The ratio of the reference and observed intensities ($I_{FTS}(\lambda)/I_{av}(\lambda)$) was used for calibration and applied to the data (Figure 3).

3. Analysis and Results

3.1. DKIST Filtergrams

Figure 1 displays coaligned images of the plage region in $H\beta$ and the G band obtained between 17:10 and 19:20 UT. Context imaging of the full Sun is provided by the AIA 1600 Å filtergram at 17:36 UT. It shows that the plage region extends toward the east limb outside the DKIST FoV. The west, north, and south borders of the DKIST FoV are surrounded by the QS. The bottom right panel shows a cutout of the AIA 1600 Å image, which is coaligned with the $H\beta/G$ -band images.

The $H\beta$ image displays multiple features including granulation, small-scale bright points, larger-scale brightenings, and dark fine-scale fibrils. Larger-scale brightenings coincide with the G band and 1600 Å bright regions suggesting that they are associated with strong MFCs known as faculae (e.g., Beck et al. 2007; Rezaei et al. 2007). Faculae are hot granules seen as a result of opacity reduction and appear brighter toward the limb (Keller et al. 2004; Berger et al. 2007). These brightenings are footpoints of plage fibrils appearing as densely packed, and mostly parallel fine-scale strands (Figure 1). The existence of both photospheric and chromospheric features in the $H\beta$

images is expected as the VBI/ $H\beta$ filter has a Lorentzian transmission profile centered at the line core and covers a significant part of the line wings, with an FWHM of ~ 0.46 Å (bottom right panel of Figure 3).

3.2. SST/CHROMIS $H\beta$ Images and Spectra

3.2.1. Overview

To investigate why and how fine-scale chromospheric features appear as high-contrast dark structures relative to the background in $H\beta$, we study the line profiles of fibrillar structures using high-resolution $H\beta$ spectral imaging obtained with CHROMIS. The top and bottom right panels in Figure 3 display CHROMIS $H\beta$ images in the line wings and core obtained at the DC. The FoV is mostly the QS with some network elements and the rosette region centered around $(x, y) = (43'', 15'')$, which is dominated by fine-scale chromospheric structures. The bottom right panel of Figure 3 shows an average QS $H\beta$ profile calculated over the relatively *fibril-free* region marked with the white box in the bottom left panel of Figure 3 with the spectral positions selected for the line scan.

3.2.2. Integration with VBI Transmission Profile

To more closely replicate the DKIST $H\beta$ filtergrams, the CHROMIS data were multiplied by the VBI transmission profile (bottom right panel of Figure 3) and integrated over the whole wavelength range covered by the spectral scan. Figure 4 shows the comparison of the resulting wavelength-integrated CHROMIS and DKIST $H\beta$ images. For a fair comparison, we have selected a region of the DKIST FoV covering a significant area of the QS. Figure 4 confirms that the wavelength-integrated CHROMIS $H\beta$ (called integrated $H\beta$ from hereon) shows similar scenes, including magnetic bright points, granular patterns, and fine-scale dark fibrillar structures as found in the VBI/ $H\beta$ filtergrams. We note that the granulation in the VBI $H\beta$ image appears more defined. This is most likely due to the fact that the CHROMIS data do not extend into the

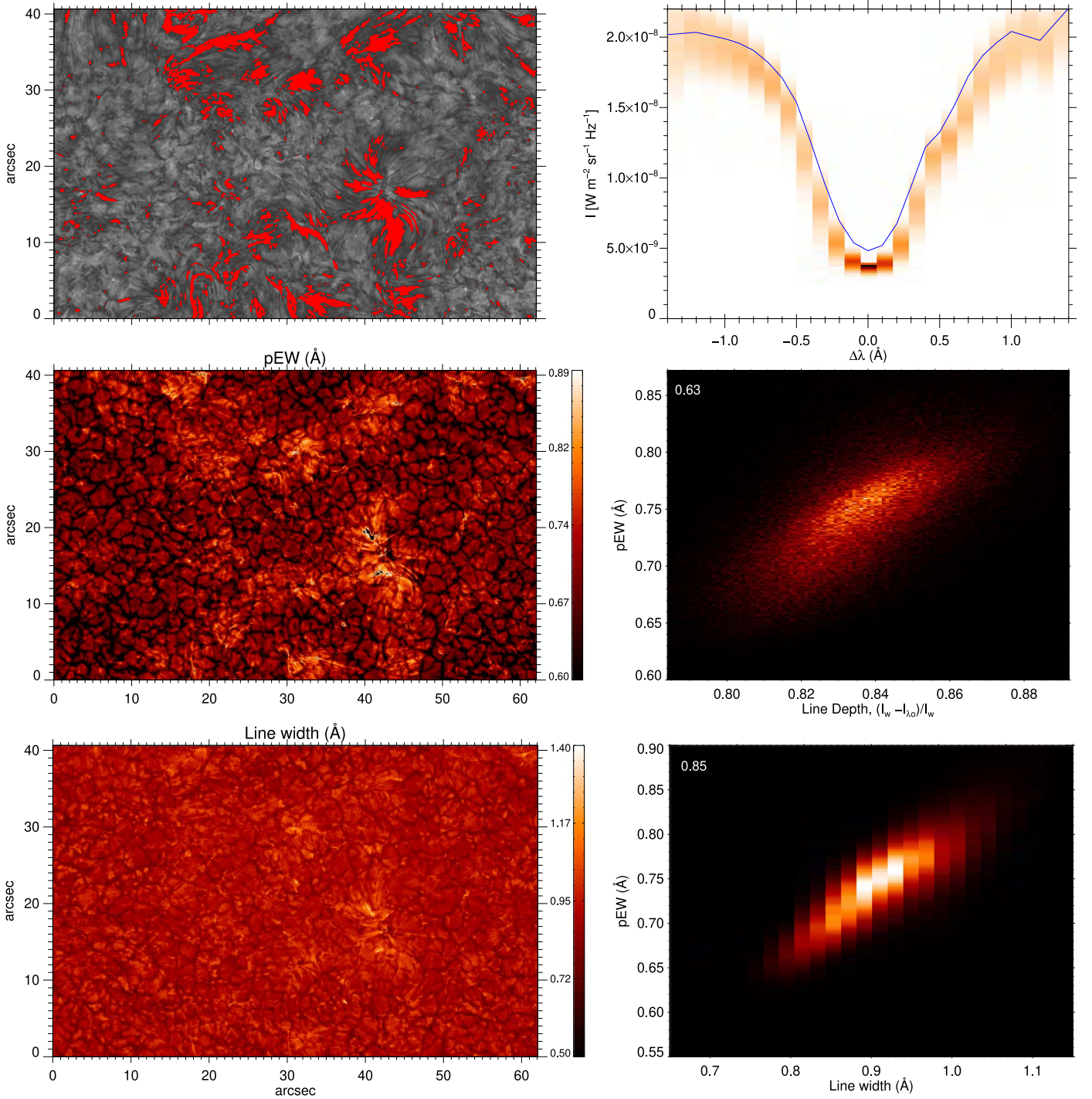


Figure 5. Top left: CHROMIS H β line core image overlaid with a mask where $I_{\lambda_0}^{\text{mean}} - I_{\lambda_0} \geq 2\sigma$ (see the text for explanation). Top right: superimposition of the extracted line profiles of detections shown in the top left panel. The average H β profile is overplotted as a blue solid line. Middle left: map of pEWs of H β line profiles measured from the double-Gaussian model. Middle right: scatter plot of the line core depths vs. pEWs for all identified fibrils. Bottom left: map of the width of H β line profiles (see the details in Section 3.2.3). Bottom right: scatter plot of the line widths vs. pEWs for all identified fibrils. The Pearson correlation coefficients are displayed in the top left corners.

continuum proper, but rather only sample up to wavelengths in the wing of the line, formed in the middle photosphere.

3.2.3. Spectral Line Parameters

To study the line profiles of fibrillar structures in the CHROMIS data we first identified them in the monochromatic line core images using simple thresholding. In particular, we

calculated the mean line profile, $(I_{\lambda_0}^{\text{mean}})$ over the fibril-free area marked with the white box in Figure 3. For line core intensities (I_{λ_0}), we applied a threshold as the mean line core intensity ($I_{\lambda_0}^{\text{mean}}$) minus 2 standard deviations (σ). The resulting detections are presented as red contours plotted over the H β line core image in the top left panel of Figure 5.

A density diagram of the line profiles has been produced with the superimposition of individual profiles from the

detections (top right panel of Figure 5). It shows that features with increased line depth also show an enhanced spectral width, with respect to the average QS profile (top right panel of Figure 5).

We applied a double-Gaussian fit to all spectral profiles to take into account the blend due to the Cr I and Th II near 4861.5 Å (at $\Delta\lambda \approx 0.4$ Å in the bottom right panel of Figure 3). We calculated the line depth $(I_w - I_{\lambda_0})/I_w$, where I_{λ_0} is the intensity of the line core and I_w is the intensity of the line wing located at $\Delta\lambda = -1.2$ Å from the line core. Due to the absence of a clear continuum reference point in the data, the line depth is calculated relative to a position in the far line wing. From the double-Gaussian model, we also calculated a parameter which we call the pseudo-equivalent width (pEW), which is a good proxy for the line equivalent width (EW). The pEW is the wavelength-integrated depression of the line profiles for each pixel over the FoV,

$$\text{pEW} = \int_{\lambda_{\text{bw}}}^{\lambda_{\text{rw}}} \frac{I_w - I_{\lambda}}{I_w} d\lambda, \quad (1)$$

where λ_{rw} and λ_{bw} correspond to the far red and blue line wing wavelengths located at $\Delta\lambda = \pm 1.2$ Å from the line core. The middle left panel of Figure 5 presents a map of the pEW showing that the detected structures have increased pEWs. The middle right panel of Figure 5 shows a scatter plot of the pEWs versus line depths for the detected fine structures revealing a correlation between these two parameters with a Pearson correlation coefficient of ~ 0.63 .

The double-Gaussian models represent well the observed line profiles. However, due to the relatively coarse spectral sampling of the data, we are not able to reliably resolve and separate Gaussian components representing H β and line blends at the red wing. To quantify the width of the H β line profiles from the SST data we followed the method used in Leenaarts et al. (2012). For each pixel in the data, we define the width of the line as the intersections of the profile and the line $I = I_{\text{min}} + (I_{\text{max}} - I_{\text{min}})/2$, where I_{min} and I_{max} are profile minimum and maximum. The bottom left panel of Figure 5 presents the map of the line width showing that the detected structures have increased line width. The bottom right panel of Figure 5 shows a scatter plot of the pEWs calculated with the double-Gaussian model versus line width. There is a clear correlation between these parameters suggesting that the pEW and line width are increased with the same line-broadening mechanism(s) and pEW is a good proxy for the line width.

3.3. Spectropolarimetric Inversions

In this section, we provide some basic information on the inversions performed on the ViSP spectropolarimetric data. A complete description will be presented in a forthcoming paper (Uitenbroek et al., in preparation).

3.3.1. Code Setup

To interpret the ViSP observations, we use the recently developed DeSire inversion code (Ruiz Cobo et al. 2022). DeSire uses the LTE inversion code Stokes Inversion based on Response functions (SIR; Ruiz Cobo & del Toro Iniesta 1994) with the forward modeling non-LTE radiative transfer solver Rybicki & Hummer (RH; Uitenbroek 2001). The code solves the multilevel non-LTE radiative transfer problem using analytical response functions derived in LTE to invert or

Table 2

Number of Cycles and Nodes Employed in the Inversions of the Ca II and Fe I Lines

Physical Parameters	Nodes Used in Different Cycles
Temperature, T	2, 5, 7, 9
Microturbulence, v_{mic}	1, 3, 3, 3
LoS velocity, v_{LoS}	2, 5, 7, 7
Magnetic field, B	2, 5, 7, 7
Inclination, γ	1, 2, 5, 5
Azimuth, ϕ	1, 2, 2, 2

synthesize photospheric and chromospheric spectral lines in 1D by assuming a plane-parallel geometry.

Prior to the inversion the observed Stokes profiles were averaged over seven and 11 pixels along the slit ($\sim 0''.208$ and $0''.213$ for arm 1 and arm 3, respectively) to equalize the vertical and horizontal scales of the pixels. The noise level of the averaged Stokes Q , U , and V profiles for Fe I and Ca II are $4.4 \times 10^{-4} I_c$ and $3.7 \times 10^{-4} I_c$, respectively. Inversions were performed in four cycles, and Table 2 summarizes the number of nodes used in the cycles. The magnetic filling factor, or the fraction of a pixel occupied by the magnetic element, is taken as $f=1$. The stratification of the atmospheric parameters obtained by the inversions is given as a function of the logarithm of the optical depth scale at 5000 Å (hereafter $\log \tau$).

3.3.2. Fe I 6301 and 6302 Å Lines

We inverted the full Stokes profiles of the Fe I 6301 and 6302 Å lines over the entire ViSP FoV. A sample plage profile with signal in all of the polarization parameters is presented in Figure 6 together with the best-fit synthetic profiles obtained from the inversion.

The inversion output showing maps of the LoS field (B_{LoS}), field strength (B), inclination (γ), azimuth (ϕ), temperature (T), and LoS velocity (v_{LoS}) at $\log \tau = -1$ (low photosphere) are presented in Figure 7. Azimuth disambiguation has not been performed for the magnetic field, and the inclination angle (γ) and azimuthal angle both describe the direction of the magnetic vector with respect to the LoS, with $\gamma=0$ defined as the direction away from the observer. In the map of B_{LoS} and B , we only consider pixels that have at least one polarization profile (Stokes Q , U , and V) with maximum absolute amplitude greater than 4 standard deviations (σ_s) (Lagg et al. 2016; Campbell et al. 2021). The inversion reveals a large inclination angle, γ , in MFCs. This is due to the large viewing angle (i.e., small μ) of the FoV, where the magnetic flux tubes that are oriented mostly along the surface normal are inclined with respect to the observer. As a result, plage MFCs have a strong magnetic field with maximum values of B greater than 2 kG, with an LoS component of only a few hundred Gauss (Figure 7). Furthermore, the maps reveal that the magnetic field of the MFCs inside the plage (see, e.g., the area within the red box in the top panels of Figure 7) is stronger than the field at the edge of the plage (area within the blue box in the top panels of Figure 7).

The map of the azimuth shows that there are dominant azimuthal directions (dark blue patches in the right panel of the second row of Figure 7) with some variations at the locations of almost all MFCs, confirming the presence of field lines aligned along the same direction. The azimuth of the magnetic field outside MFCs is not well defined as there are very weak Q and

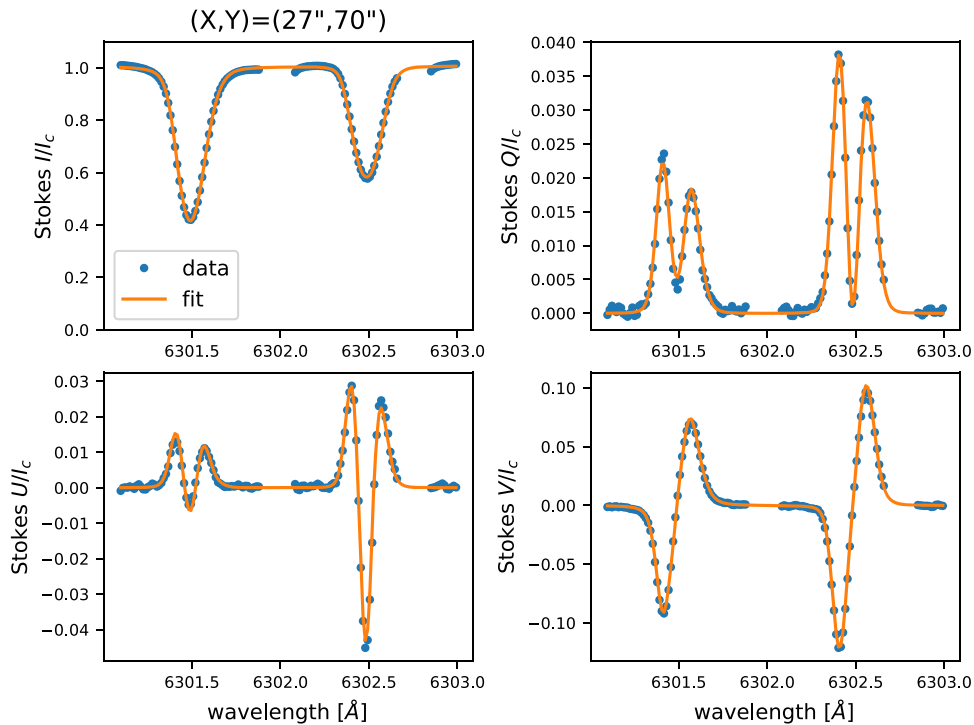


Figure 6. A typical set of Fe I 6301/6302 Å Stokes profiles with corresponding well-fitting synthetic profiles obtained from the inversion. The selected pixels have successfully fitted Stokes profiles with the realistic atmospheric model. The two O₂ telluric lines have been removed from the observed Fe I 6302 Å spectra.

U signals. A temperature map of the inverted region shows temperature enhancements for MFCs at $\log \tau = -1$ (Figure 7). The plage elements exhibit enhanced temperatures, similar to their appearance in the G -band images. The LoS velocity map indicates that there is a suppressed granular convection (abnormal granulation) in the plage MFCs (Figure 7).

3.3.3. Inclination Map

Figure 8 shows a coaligned $H\beta$ image and an inclination map at $\log \tau = -1.8$, corresponding to the middle photosphere. The P1–P3 boxes in Figure 8 mark selected regions of the MFCs within the plage. The boxes are split into red and blue boxes that mark roughly the fibrils directed toward the observer (red boxes) and away from the observer (blue boxes). The direction of the DC is indicated by the blue arrows. Histograms of the field inclination within these boxes indicate that magnetic flux tubes associated with the lower parts of away-directed fibrils (toward the limb) are less inclined than flux tubes of fibrils directed toward the observer (toward the DC; see the bottom panels of Figure 8). We discuss these findings in Section 4.

3.4. Ca II 8542 Å Line

We invert the Ca II 8542 Å (hereafter Ca II) together with the photospheric Si I 8536 Å and Fe I 8538 Å lines located in the blue wing of the Ca II line. A five bound level-plus-continuum Ca II model atom with complete angle and frequency redistribution is used. The Stokes Q and U signals in the chromosphere are inherently weak and the noise level in these data prevents their reliable inversions.

The top row of Figure 9 presents maps of the Ca II Stokes I at line core and Stokes V at $\Delta\lambda = -0.2$ Å, for the full FoV covered by ViSP scans at four adjacent pointings. Due to the

shorter length of the ViSP slit in this spectral arm (Table 1), there is a gap between the upper and lower merged raster scans. These maps show that the enhancement of circular polarization signals (Stokes V) is cospatial with the MFCs and fibrils directed toward the LoS in the intensity maps (Stokes I) (Figure 9).

Representative examples of Stokes profiles with the best-fitting synthetic profiles obtained from the inversion for the pixels located in a strong MFC and a fibril outside MFCs are presented in Figure 10. The inversion output showing the maps of temperature, LoS magnetic field, mass density, and LoS velocity, integrated between $\log \tau = -2.8$ and -4.3 , are presented in the middle and bottom rows of Figure 9. The temperature map derived from the inversions (middle row, left column in the Figure) shows clear temperature enhancements in correspondence with the MFCs, but over larger, more diffuse areas than for the photospheric case (Figure 7). The LoS velocity map of the same region reveals weak downflows along the area where chromospheric fibrillar features are located (Figure 9).

4. Discussion

We investigated the fine-scale structure of the plage chromosphere by analyzing broadband imaging and full Stokes spectropolarimetric observations in the $H\beta$, Ca II 8542 Å, and Fe I 6301/6302 Å lines obtained with the largest solar optical telescope, DKIST. Plages are unipolar magnetic regions appearing either in the vicinity of strong ARs with sunspots or smaller remnants of decayed unipolar ARs without sunspots (e.g., Rutten 2021). We observed a non-sunspot-associated plage located at around $(x, y) = (-362'', -406'')$. The large FoV of DKIST covered most of the plage including its boundaries with the QS (Figures 1 and 2).

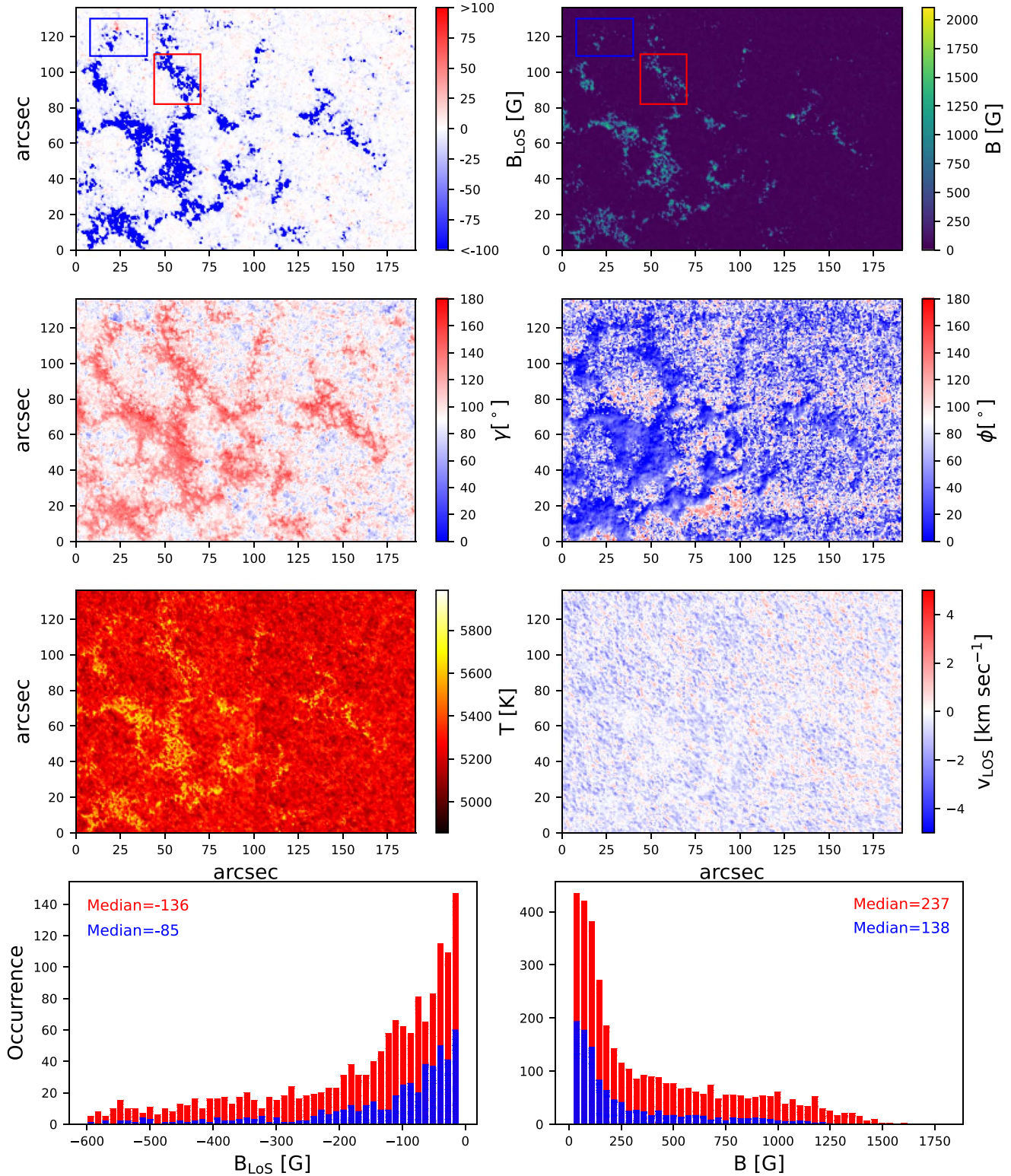


Figure 7. Results of the spectral inversions for the Fe I 6301 and 6302 Å lines, showing the LoS magnetic field, the field strength, inclination, azimuth, temperature, and LoS velocity maps at $\log \tau = -1$. The bottom panels depict histograms of the LoS magnetic field and magnetic field strength for all pixels with negative B_{LoS} inside the areas marked with the red and blue boxes in the top row. Median values are displayed in the top corners.

4.1. The Appearance of $H\beta$ Fibrils

The VBI $H\beta$ images are dominated by very prominent, fine-scale, densely packed fibrils that are mostly parallel to each

other (Figure 1) and are anchored at the unipolar, extended photospheric MFCs (Figure 2). To understand their appearance, we employed high-resolution spectral imaging data obtained

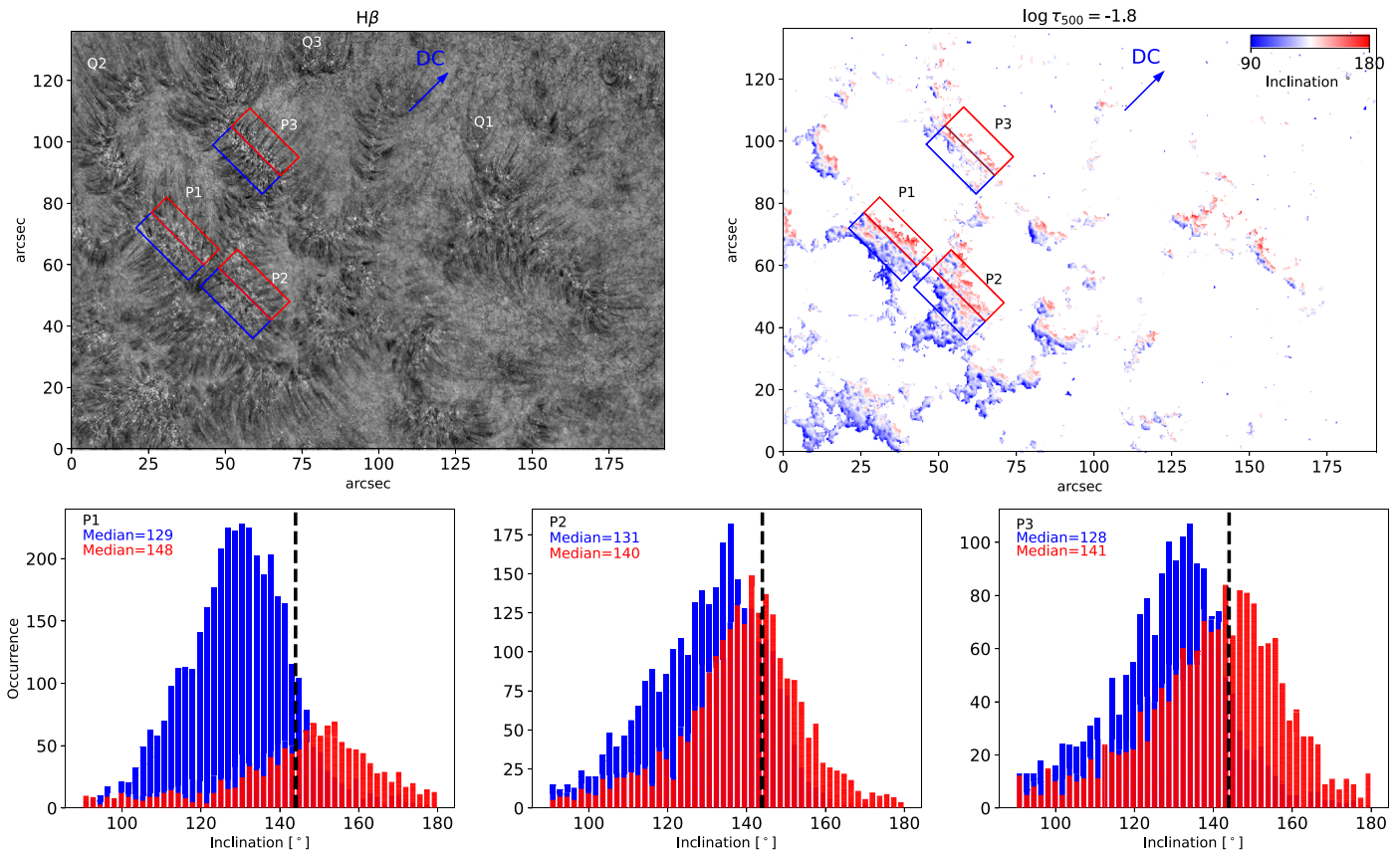


Figure 8. Coaligned VBI $H\beta$ image and inclination map produced with the inversion of ViSP Fe I 6301/6302 Å lines. Q1–Q3 mark areas where fibrils are oriented preferably toward the QS. P1–P3 boxes mark the fibrils that are directed away from the observer (blue boxes) and toward the observer (red boxes) inside the plage. Inclination angle histograms of the areas marked with blue and red boxes for the P1–P3 regions are presented in the bottom panels with blue and red bars. Median values are also displayed in the top left corners. The inclination map and histograms only include pixels with a maximum absolute amplitude of the Stokes parameter more than $4\sigma_s$ (see the text for an explanation). The vertical lines mark the inclination angles between LoS and local vertical ($\gamma \approx 144^\circ$).

with SST/CHROMIS on a comparable target, and studied their spectral properties (Figure 3). By multiplying the CHROMIS spectral imaging data with the VBI transmission profile and averaging over the sampled wavelengths, we are able to reproduce the $H\beta$ scene found in the VBI data (Figure 4). The analysis shows that the dark, fibrillar structures seen in the composite CHROMIS data have both increased line width and line depth with respect to the average QS profile (Figure 5), explaining why these features appear as high-contrast dark structures relative to the background in the VBI $H\beta$ image.

4.2. Opacity Broadening of the Fibrils $H\beta$ Line Width

The line broadening of chromospheric fine structures is a well-known phenomenon that has been reported in many observations (see the reviews by Beckers 1972; Tsiropoula et al. 2012). However, establishing the exact reasons for the line broadening remains a central problem of chromospheric research. The increased line width can be caused by increased local temperatures produced by thermal and nonthermal heating processes, nonthermal motions, turbulence, and MHD waves. These mechanisms have been investigated in recent decades using both advanced theoretical modeling and high-resolution, multi-instrument observations but a definitive explanation still eludes us.

Another broadening mechanism relevant to chromospheric spectral lines is opacity broadening. Increased opacity could enhance the absorption in the line core/inner wing and hence

broaden the line width. This could also cause a larger line core depth if the line core intensity is not saturated. The latter scenario is encountered when the observed layer/structure in the chromosphere is optically thin (Rutten 2003). In this regime, there is a strong correlation between line core optical depth and EW through the curve of growth.

Due to the absence of a clear continuum in our data, we are not able to calculate EWs for the $H\beta$ line. Instead, we measured the line depression integrated over the wavelength range of the CHROMIS spectral scan. This parameter (called pEW) can be taken as a good proxy of the EW and line width (Figure 5). The maps of the pEWs and line width show that the detected fibrillar structures have increased pEWs, line widths, and variable line core depths (Figure 5). Furthermore, the scatter plot of the pEW versus line depth reveals a clear correlation between these two parameters (middle right panel of Figure 5). This suggests that the optical thickness of fibrils in the $H\beta$ line center is less than 1, which classifies the fibril plasma as optically thin in this line, and not much larger than 1 ($\tau \gtrsim 1$). In such conditions, the fibril’s line width and depth are very sensitive to the optical depth and hence opacity broadening can make a significant contribution to the observed line broadening. Opacity broadening of plage fibrils in the $H\alpha$ line has been discussed in Molnar et al. (2019) where they proposed that the broadening could be due to an increased population number of the first excited level of hydrogen, due to an enhanced downward Ly α wing flux. They concluded that this population

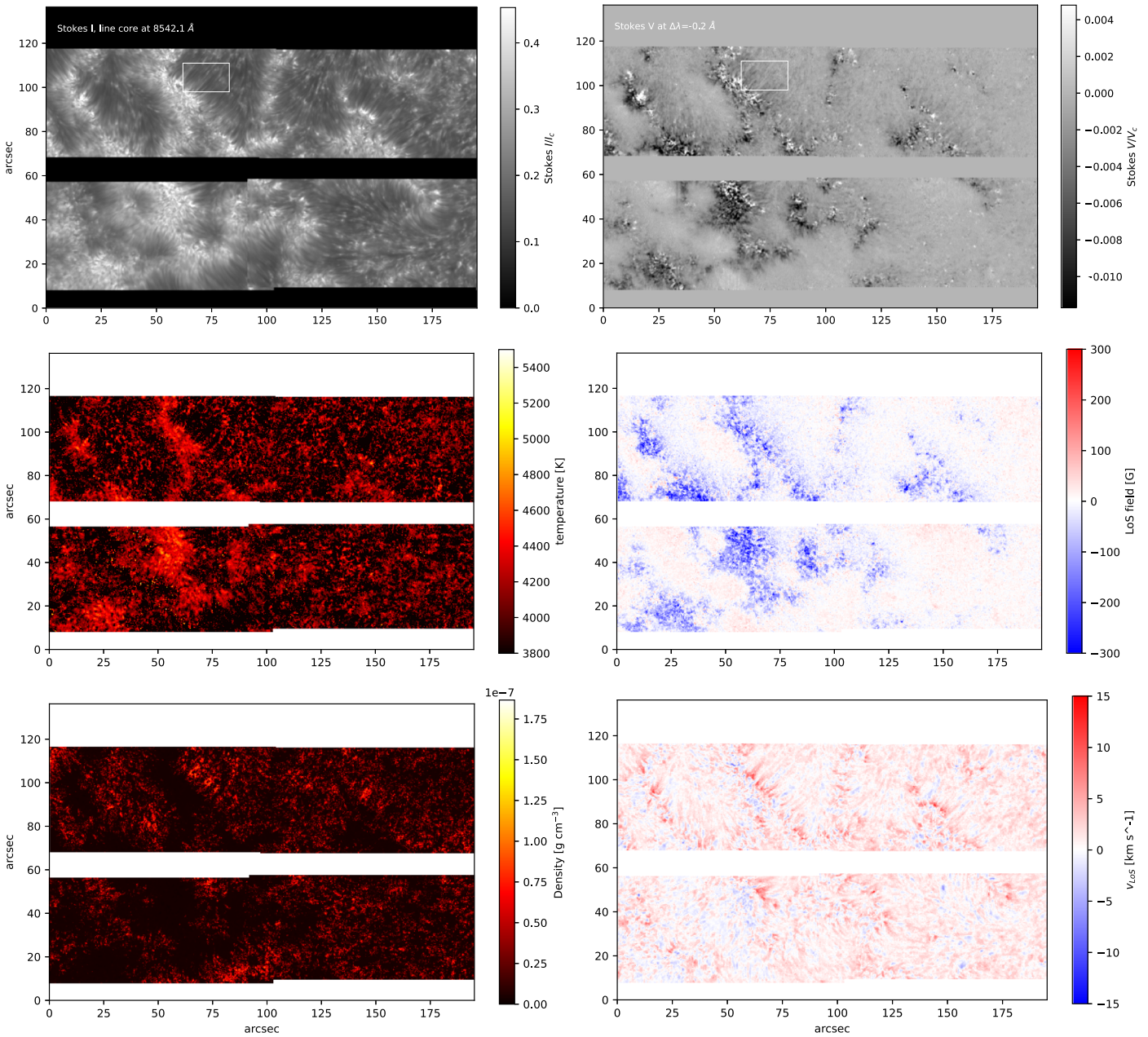


Figure 9. The top panels show the ViSP images in the Ca II 8542 Å Stokes I line core and Stokes V at $\Delta\lambda = -0.2$ Å. The DeSIRE output showing the temperature, LoS magnetic field, mass density, and LoS velocity maps averaged over the interval between $\log \tau = -2.8$ and -4.3 are presented in the middle and bottom panels. The white boxes mark an area where fibrils are oriented toward the LoS direction.

number can be affected significantly by the downward Ly α wing flux.

Leenaarts et al. (2012) showed that the H α opacity in the upper chromosphere calculated using radiation-MHD simulations and three-dimensional non-LTE radiative transfer computations is mainly sensitive to the mass density and only weakly sensitive to the temperature. They showed that enhanced chromospheric mass density in fibrils pushes the line formation height upward where the source function is set by the horizontal average of the angle-averaged radiation field. On the other hand, the radiation field is independent of the local temperature and decreases as a function of height. As a result fibrils appear dark in H α against their deeper-formed background (Leenaarts et al. 2012). Increased opacity in the H β line, manifest as increased line depth and width, could be

related to the increased density in fibrils, with respect to their background atmosphere.

In contrast to H β , no correlation between line core intensity and line width of H α has been reported by Cauzzi et al. (2009) (see Figure 6 therein). This difference is not surprising as the H α is more optically thick. The oscillator strength of the H α transition is around seven times larger than the oscillator strength of the H β transition. Therefore, the H α line core intensity for fibrils should saturate faster with increased opacity. In our data, we note that despite a clear linear tendency, the scattered data points (middle right panel of Figure 5) indicate that the spectra of some H β structures can be in the saturation (optically thick) regime and/or other broadening mechanisms that are dominant in some fibrils.

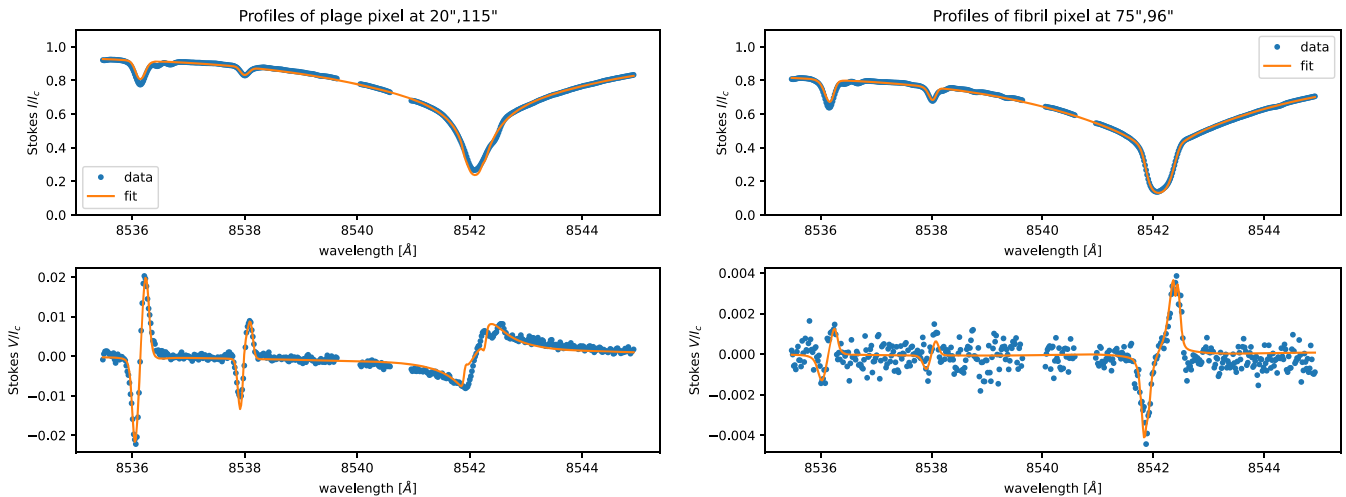


Figure 10. Typical set of Stokes profiles with corresponding well-fitting synthetic profiles obtained from the inversion of a pixel located in a strong MFC (left panels) and a pixel in a fibril outside of MFCs (right panels). These selected pixels have Stokes V successfully fitted with the realistic atmospheric model. The two H_2O telluric lines have been removed from the observed Ca II 8542 Å spectra.

4.3. Morphology of Fibrils and Magnetic Canopy

It is widely accepted that fibrils are preferentially formed along continuous lines of magnetic force with their footpoints rooted into the photospheric MFCs. Our observations show that $\text{H}\beta$ fibrils within the plage appear shorter compared to fibrils at the edge of the plage, parallel to each other, and directed to both sides of the extended MFCs (see, e.g., regions marked with P1, P2, P3 in Figure 8). However, they appear longer and are directed preferably toward the QS regions near the edge of the plage (see regions marked with Q1, Q2, and Q3 in Figure 8). Similar results for plage fibrils observed in $\text{H}\alpha$ and Ca II K filtergrams have been reported by Foukal (1971a, 1971b) and Pietarila et al. (2009). Some limitations related to our inversions, such as large viewing angle, lack of knowledge of exact geometrical heights, limited FoV, and low S/N for linear polarizations in the chromosphere, hinder the determination of the 3D geometry of the flux tubes and the height where the magnetic canopy is merging in different part of the plage.

The maps of total magnetic field strength and LoS magnetic field in the photosphere at $\log \tau = -1$ obtained from the inversion of the Fe I 6301/6302 Å lines show that there are larger MFCs located close to each other inside the plage (Figure 7), hence a smaller separation between MFCs inside the plage than at its edges. Following Durrant (1988) and Martínez Pillet et al. (1997) we can define a *magnetic filling factor*, f_l^4 , at a reference photospheric height. The canopies of neighboring MFCs merge at a distance above the reference level given by the analytical formula, $z_m \approx -2H \ln f_l$, where z_m is the height at which the canopy merges, H is the pressure scale height of the isothermal atmosphere. Assuming that the scale height of the plage MFCs is approximately the same everywhere, z_m has to be lower inside the plage. A low-lying canopy with funnel-like cross section can explain why fibrils are shorter inside the plage (Figure 11).

At the edges of plage regions, the magnetic field strength of MFCs is weaker than the field strength of neighboring MFCs inside the plage (Figure 7). As a result, the funnel-like magnetic

field configuration can be bent away from the plage toward the edge of the plage and QS to compensate for the lateral magnetic pressure imbalance (Figure 11). This could explain why observed fibrils at the edges of the plage have a preferred orientation toward the QS (see regions marked with Q1–Q3 in Figure 8).

Maps of the inclination angle reveal that flux tubes at the lower parts of fibrils directed toward the observer (toward the DC) have a larger inclination angle (γ) than flux tubes of fibrils directed away from the observer (toward the limb) (Figure 8). This is manifested in the histograms comparing the distribution of inclination angle for blue and red boxes marking lower parts of fibrils directed toward the DC and limb, respectively (Figure 8). The average heliocentric angle of the regions marked with P1–P3 is 36° ($\mu \approx 0.8$). Therefore, flux tubes aligned along the local vertical should have $\gamma \sim 144^\circ$ inclination. The strongest magnetic field patches inside MFCs have a median inclination close to 144° . However, the histograms of Figure 8 show that the inclination angle with respect to 144° (local vertical) for areas marked with red and blue boxes have different distributions and median values. This could be an indication that flux tubes are beginning to diverge from the vertical at photospheric heights as they form a magnetic canopy in the upper atmosphere (Figure 11).

4.4. The Chromospheric Models

The Stokes V images of Ca II at $\Delta\lambda = -0.2$ Å and the LoS magnetic field map obtained from inversion of the Ca II spectra show that the enhancement in circular polarization and B_{LoS} outside the MFCs is detected in the areas where fibrils are oriented toward the LoS (North-west) direction (see region marked with the white boxes in the top panels of Figure 9). Figure 10 compares the Stokes I and V profiles of representative pixels located on the plage MFC and fibril. The Stokes V of MFC shows a strong signal at the Si I 8536 Å and Fe I 8538 Å photospheric lines as well as in the Ca II chromospheric line, indicating that the plage MFC is dominated by both photospheric and chromospheric magnetic field components. However, the fibril pixels only show strong Stokes V for the Ca II line, suggesting the presence of the purely chromospheric magnetic field. Given the large viewing

⁴ We note the filling factor introduced here is not the same as the filling factor used in the inversions. Here f_l is the large-scale filling factor defined by the separation of MFCs whereas in the inversions the filling factor is defined within a resolution element.

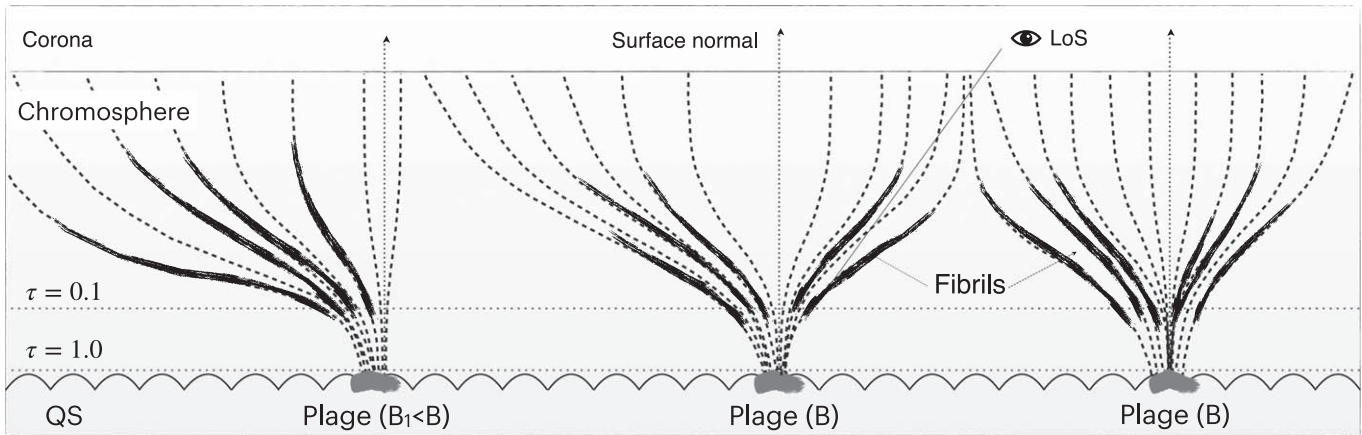


Figure 11. Schematic representation of the unipolar plage magnetic field configuration showing the basic geometry of the fibrils inside and at the boundaries of the plage. Unipolar strong MFCs close to each other inside the plage create low-lying canopy/flux tubes with funnel-like cross-sections and shorter fibrils. At the edges of plage where $B_1 < B$, magnetic field lines can be pushed away toward the edge of the plage and QS. This creates an asymmetric configuration of the funnel-like canopy where flux tubes and fibrils from the edge of the plage are directed preferably toward the QS. Dotted horizontal lines mark the base of the photosphere ($\tau = 1$) and the upper photospheric layer ($\tau = 0.1$) where Fe I 6301/6302 Å lines have a high sensitivity.

angle for this region, the strong signal in Stokes V implies a large inclination of the field with respect to the local vertical.

Fibrils appear dominated by redshifted plasma in the LoS velocity map (bottom right panel of Figure 9) suggesting the presence of gravity-driven downflows from the top of the fibril toward the footpoints. The domination of downflows indicates that plage fibrils observed in Ca II are cool and dense plasma which in turn supports the opacity broadening discussed earlier. Interestingly, the map of mass density derived from the spectral inversions displays areas of enhanced density in the plage fibrils (bottom left panel of Figure 9). Although one has to be cautious in interpreting such a map, as the density is derived from the assumption of hydrostatic equilibrium, this represents a tantalizing clue on the nature of the fibrils, that will deserve further investigation.

Finally, we note that field-aligned, rapid chromospheric plasma downflows along spicules have been recently reported by Bose et al. (2021). By analyzing their morphological and dynamical properties, Bose et al. (2021) suggested that the detected downflows might be the chromospheric counterparts of the frequently observed redshifts/downflows predominantly seen in the TR/low coronal lines (Doscchek et al. 1976; Dadashi et al. 2011).

5. Concluding Remarks

High-resolution $H\beta$ filtergrams obtained with DKIST/VBI show that the plage chromosphere is dominated by fine-scale fibrils. Due to their enhanced line width and line depth, the fibrillar features are clearly visible in both broadband filtergrams as well as in monochromatic line core and wing images. This demonstrates that $H\beta$ observations are an excellent diagnostic to identify and track fine-scale structures in the chromosphere.

Our results also suggest that $H\beta$ fibrils can be optically thin structures, making this line a very appropriate choice for the well-known cloud modeling inversion proposed originally by Beckers (1964). Cloud modeling remains one of the most important inversion techniques for the Balmer lines and works at its best for optically thin structures (Tziotziou 2007).

A correlation between the $H\beta$ line depth and width indicates that opacity broadening could be the main reason for the spectral

line broadening observed frequently in spicules and fibrils. Whether this mechanism is supported by an increase in electron density due to enhanced Ly α flux as proposed by Molnar et al. (2019) or by an overall increase in density as proposed by Leenaarts et al. (2012), remains to be determined. It is possible that footpoint heating, manifested as a temperature enhancement of the MFCs (Figures 7 and 9) could lead to hot plasma upflows in the chromosphere along magnetic flux tubes; rapid cooling of this plasma through radiation losses could then lead to the formation of denser fibrils, consistent with the pervasive downflows observed in the Ca II 8542 Å line (Figure 8). Hot plage fibril footpoints have been reported recently by Kriginsky et al. (2023) using spectral inversions of the same line. Semiempirical models constructed from the inversions seem to indicate the existence of dense fibrils dominated by downflowing plasma in the Ca II 8542 Å line. However, assessing the exact contribution of the opacity broadening in the fibril line widths requires advanced radiative magnetohydrodynamic computations including synthesizing fibril spectra in $H\beta$. This will be studied in a future paper where we plan to perform 3D, non-LTE radiative transfer calculations of the $H\beta$ line.

The analyses of photospheric and chromospheric polarization data show that morphological characteristics, such as orientation, inclination, and the length of fibrils, are defined by the topology of the magnetic field in the lower solar atmosphere. Future DKIST observations with improved S/N for linear polarization signals in chromospheric lines will provide vector magnetograms for the 3D geometry of the plage chromosphere.

Acknowledgments













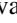

The research reported herein is based in part on data collected with DKIST a facility of the National Science Foundation. DKIST is operated by the National Solar Observatory under a cooperative agreement with the Association of Universities for Research in Astronomy, Inc. DKIST is located on land of spiritual and cultural significance to Native Hawaiian people. The use of this important site to further scientific knowledge is done so with appreciation and respect. D.K. thanks V. Martínez Pillet and T. Zaqarashvili for helpful discussions. D.K. acknowledges the Georgian Shota Rustaveli National Science

Foundation project FR-22-7506. D.K. acknowledges the Science and Technology Facilities Council (STFC) grant ST/W000865/1. M.M. and R.J.C. acknowledge support from STFC under grants ST/P000304/1, ST/T001437/1, ST/T00021X/1, and ST/X000923/1. The 1 m SST is operated on the island of La Palma by the Institute for Solar Physics of Stockholm University in the Spanish Observatorio del Roque de los Muchachos of the Instituto de Astrofísica de Canarias. The Institute for Solar Physics is supported by a grant for research infrastructures of national importance from the Swedish Research Council (registration number 2017-00625).

Facilities: DKIST (VBI and ViSP), SST (CHROMIS), SDO (AIA and HMI).

Software: DeSIRE (Ruiz Cobo et al. 2022), *ad hoc*_talk (Jaeggli et al. 2022).

ORCID iDs

David Kuridze  <https://orcid.org/0000-0003-2760-2311>
 Han Uitenbroek  <https://orcid.org/0000-0002-2554-1351>
 Friedrich Wöger  <https://orcid.org/0000-0001-6907-9739>
 Mihalis Mathioudakis  <https://orcid.org/0000-0002-7725-6296>
 Huw Morgan  <https://orcid.org/0000-0002-6547-5838>
 Ryan Campbell  <https://orcid.org/0000-0001-5699-2991>
 Catherine Fischer  <https://orcid.org/0000-0001-9352-3027>
 Gianna Cauzzi  <https://orcid.org/0000-0002-6116-7301>
 Thomas Schad  <https://orcid.org/0000-0002-7451-9804>
 Kevin Reardon  <https://orcid.org/0000-0001-8016-0001>
 João M. da Silva Santos  <https://orcid.org/0000-0002-3009-295X>
 Christian Beck  <https://orcid.org/0000-0001-7706-4158>
 Alexandra Tritschler  <https://orcid.org/0000-0003-3147-8026>
 Thomas Rimmele  <https://orcid.org/0000-0002-7213-9787>

References

- Anan, T., Kitai, R., Kawate, T., et al. 2010, *PASJ*, **62**, 871
 Anan, T., Schad, T. A., Kitai, R., et al. 2021, *ApJ*, **921**, 39
 Beck, C., Bellot Rubio, L. R., Schlichenmaier, R., & Sütterlin, P. 2007, *A&A*, **472**, 607
 Beck, C., Gosain, S., & Kiessner, C. 2019, *ApJ*, **878**, 60
 Beck, C., Rezaei, R., Puschmann, K. G., & Fabbian, D. 2016, *SoPh*, **291**, 2281
 Beckers, J. M. 1964, PhD thesis, Univ. Utrecht
 Beckers, J. M. 1968, *SoPh*, **3**, 367
 Beckers, J. M. 1972, *ARA&A*, **10**, 73
 Berger, T. E., Rouppe van der Voort, L., & Löfdahl, M. 2007, *ApJ*, **661**, 1272
 Bernasconi, P. N., Keller, C. U., Povel, H. P., & Stenflo, J. O. 1995, *A&A*, **302**, 533
 Bose, S., Joshi, J., Henriques, V. M. J., & Rouppe van der Voort, L. 2021, *A&A*, **647**, A147
 Buehler, D., Lagg, A., Solanki, S. K., & van Noort, M. 2015, *A&A*, **576**, A27
 Buehler, D., Lagg, A., van Noort, M., & Solanki, S. K. 2019, *A&A*, **630**, A86
 Campbell, R. J., Mathioudakis, M., Collados, M., et al. 2021, *A&A*, **647**, A182
 Carlsson, M., De Pontieu, B., & Hansteen, V. H. 2019, *ARA&A*, **57**, 189
 Cauzzi, G., Reardon, K., Rutten, R. J., et al. 2009, *A&A*, **503**, 577
 da Silva Santos, J. M., Reardon, K., Cauzzi, G., et al. 2023, *ApJL*, **954**, L35
 Dadashi, N., Teriaca, L., & Solanki, S. K. 2011, *A&A*, **534**, A90
 de la Cruz Rodríguez, J., & van Noort, M. 2017, *SSRv*, **210**, 109
 de Pontieu, B., McIntosh, S., Hansteen, V. H., et al. 2007, *PASJ*, **59**, S655
 De Pontieu, B., McIntosh, S. W., Carlsson, M., et al. 2011, *Sci*, **331**, 55
 de Wijn, A. G., Casini, R., Carlile, A., et al. 2022, *SoPh*, **297**, 22
 Doschek, G. A., Feldman, U., & Bohlin, J. D. 1976, *ApJL*, **205**, L177
 Durrant, C. J. 1988, *The Atmosphere of the Sun* (Bristol: Hilger)
 Erdélyi, R., & Fedun, V. 2007, *Sci*, **318**, 1572
 Foukal, P. 1971a, *SoPh*, **19**, 59
 Foukal, P. 1971b, *SoPh*, **20**, 298
 Henriques, V. M. J., Kuridze, D., Mathioudakis, M., & Keenan, F. P. 2016, *ApJ*, **820**, 124
 Jaeggli, S. A., Schad, T. A., Tarr, L. A., & Harrington, D. M. 2022, *ApJ*, **930**, 132
 Jess, D. B., Mathioudakis, M., Erdélyi, R., et al. 2009, *Sci*, **323**, 1582
 Keller, C. U., Schüssler, M., Vögler, A., & Zakharov, V. 2004, *ApJL*, **607**, L59
 Kriginsky, M., Oliver, R., & Kuridze, D. 2023, *A&A*, **672**, A89
 Kuridze, D., Henriques, V., Mathioudakis, M., et al. 2015, *ApJ*, **802**, 26
 Kuridze, D., Morton, R. J., Erdélyi, R., et al. 2012, *ApJ*, **750**, 51
 Kuridze, D., Socas-Navarro, H., Koza, J., & Oliver, R. 2021, *ApJ*, **908**, 168
 Kuridze, D., Zaqarashvili, T. V., Henriques, V., et al. 2016, *ApJ*, **830**, 133
 Lagg, A., Solanki, S. K., Doerr, H. P., et al. 2016, *A&A*, **596**, A6
 Langangen, Ø., De Pontieu, B., Carlsson, M., et al. 2008, *ApJL*, **679**, L167
 Leenaarts, J., Carlsson, M., & Rouppe van der Voort, L. 2012, *ApJ*, **749**, 136
 Lemen, J. R., Title, A. M., Akin, D. J., et al. 2012, *SoPh*, **275**, 17
 Löfdahl, M. G., Hillberg, T., de la Cruz Rodríguez, J., et al. 2021, *A&A*, **653**, A68
 Madjarska, M. S., Vanninathan, K., & Doyle, J. G. 2011, *A&A*, **532**, L1
 Martínez Pillet, V., Lites, B. W., & Skumanich, A. 1997, *ApJ*, **474**, 810
 Molnar, M. E., Reardon, K. P., Chai, Y., et al. 2019, *ApJ*, **881**, 99
 Morosin, R., de la Cruz Rodríguez, J., Vissers, G. J. M., & Yadav, R. 2020, *A&A*, **642**, A210
 Neckel, H. 1999, *SoPh*, **184**, 421
 Pietarila, A., Hirzberger, J., Zakharov, V., & Solanki, S. K. 2009, *A&A*, **502**, 647
 Pietrow, A. G. M., Kiselman, D., de la Cruz Rodríguez, J., et al. 2020, *A&A*, **644**, A43
 Prasad, A., Ranganathan, M., Beck, C., et al. 2022, *A&A*, **662**, A25
 Rezaei, R., Schlichenmaier, R., Beck, C. A. R., et al. 2007, *A&A*, **466**, 1131
 Rimmele, T. R., Warner, M., Keil, S. L., et al. 2020, *SoPh*, **295**, 172
 Roberts, W. O. 1945, *ApJ*, **101**, 136
 Rouppe van der Voort, L., Leenaarts, J., de Pontieu, B., et al. 2009, *ApJ*, **705**, 272
 Ruiz Cobo, B., & del Toro Iniesta, J. C. 1994, *A&A*, **283**, 129
 Ruiz Cobo, B., Quintero Noda, C., Gafeira, R., et al. 2022, *A&A*, **660**, A37
 Rutten, R. J. 2003, *Radiative Transfer in Stellar Atmospheres*
 Rutten, R. J. 2021, arXiv:2103.02369
 Scharmer, G. 2017, in *SOLARNET IV: The Physics of the Sun from the Interior to the Outer Atmosphere*, 85 (La Laguna: Instituto de Astrofísica de Canarias)
 Scharmer, G. B., Bjelksjo, K., Korhonen, T. K., et al. 2003, *Proc. SPIE*, **4853**, 341
 Scherrer, P. H., Schou, J., Bush, R. I., et al. 2012, *SoPh*, **275**, 207
 Secchi, A. 1877, *Le Soleil* (Paris: Gauthier-Villars)
 Spruit, H. C. 1976, *SoPh*, **50**, 269
 Sterling, A. C. 2000, *SoPh*, **196**, 79
 Topka, K. P., Tarbell, T. D., & Title, A. M. 1992, *ApJ*, **396**, 351
 Trujillo Bueno, J., & del Pino Alemán, T. 2022, *ARA&A*, **60**, 415
 Tsiropoula, G., Tziotziou, K., Kontogiannis, I., et al. 2012, *SSRv*, **169**, 181
 Tziotziou, K. 2007, in *ASP Conf. Ser. 368, The Physics of Chromospheric Plasmas*, ed. P. Heinzel, I. Dorotović, & R. J. Rutten (San Francisco, CA: ASP), 217
 Uitenbroek, H. 2001, *ApJ*, **557**, 389
 Van Noort, M., Rouppe Van Der Voort, L., & Löfdahl, M. G. 2005, *SoPh*, **228**, 191
 Wöger, F. 2014, *Proc. SPIE*, **9147**, 914791
 Wöger, F., Rimmele, T., Ferayorni, A., et al. 2021, *SoPh*, **296**, 145
 Wöger, F., von der Lühe, O., & Reardon, K. 2008, *A&A*, **488**, 375
 Zaqarashvili, T. V., & Erdélyi, R. 2009, *SSRv*, **149**, 355